Insight into the effect of A-site cations on structural and optical properties of RE$_2$Hf$_2$O$_7$:U nanoparticles

Maya Abdou[a], Santosh K. Gupta[a,b], Jose P. Zuniga[a], Yuanbing Mao[a,c,*]

[a] Department of Chemistry, University of Texas Rio Grande Valley, 1201 West University Drive, Edinburg, TX, 78539, USA
[b] Radiochemistry Division, Bhabha Atomic Research Centre, Trombay, Mumbai, 400085, India
[c] School of Earth, Environmental, and Marine Sciences, University of Texas Rio Grande Valley, 1201 West University Drive, Edinburg, TX, 78539, USA

ABSTRACT

A$_2$B$_2$O$_7$ type pyrochlores have been recently proposed as a potential nuclear waste host due to their many interesting properties. To assess and understand the performance of these compounds as nuclear waste hosts, the speciation and structural investigations on actinide-doped RE$_2$Hf$_2$O$_7$ are needed since both are imperative from their application perspective. In this work, we investigated the effect of uranium doping at different concentrations in the range of 0–10% on the structural and optical properties of RE$_2$Hf$_2$O$_7$:U (RE = Y, Gd, Nd, and Lu) nanoparticles (NPs). The Y$_2$Hf$_2$O$_7$ NPs exist in slightly disordered pyrochlore structure and the extent of disordering increases as a function of uranium doping while the structure reaches a cotunnite phase at 10.0% doping level. The Nd$_2$Hf$_2$O$_7$ NPs also exist in a distorted pyrochlore structure and their distortion increases with increasing uranium doping inducing a phase transition into a disordered fluorite structure at 10.0% uranium doping. Both Gd$_2$Hf$_2$O$_7$ and Lu$_2$Hf$_2$O$_7$ NPs exist in a disordered fluorite structure and transforms into cotunnite structure at higher U concentrations ($\geq$ 5.0%). Photoluminescence spectroscopy showed that uranium ions are stabilized in +6 oxidation state in all samples: in the form of uranate ion UO$_6$$^{6-}$ in the Y$_2$Hf$_2$O$_7$, Nd$_2$Hf$_2$O$_7$ and Lu$_2$Hf$_2$O$_7$ NPs while in the form of uranyl ion UO$_2$$^{2+}$ in the Gd$_2$Hf$_2$O$_7$ NPs. Therefore, this work deepens the understanding of the behavior of uranium ions doped in different RE$_2$Hf$_2$O$_7$ host matrices in the perspective of their application as nuclear waste hosts.

1. Introduction

Photophysical properties of actinides are highly enriching and interesting. This is mainly attributed to different properties of 5f electrons compared to 4f electrons. Actinide ions have large spin orbit coupling compared to lanthanides, and therefore relatively closed by J levels which can lead to high probability of non-radiative transition. Moreover, 5f orbitals have more spatial extension than 4f and hence they are much more sensitive to crystal/ligand field, symmetry, and coupling to external modes. This results in broader emission and shorter lifetime. The photophysical properties of uranium is not only important from the fundamental understanding point of view, but it can also give deeper insight into immobilization of nuclear waste and more so in pyrochlore ceramic matrix with an A$_2$B$_2$O$_7$ formula as a host.

As a special set of A$_2$B$_2$O$_7$ compounds, rare earth hafnate RE$_2$Hf$_2$O$_7$ pyrochlores have attracted intensive interest in the past decade because of their interesting properties such as low thermal conductivity, high dielectric constant, high density, high effective atomic number,

interesting electrical properties, high radiation stability, high phase stability, and tendency to exhibit order-disorder phase transition, etc. [1–4] These properties make them ideal candidates for applications in thermal barrier coatings [5], high k-dielectrics [6], scintillators [7], positron emission tomography [8], nuclear waste hosts [2], luminescence hosts [9], and solid oxide fuel cells [10]. It is reported that pyrochlores with A$_2$B$_2$O$_7$ composition are highly promising for immobilizing various high-level wastes containing fissile elements ([239]Pu and [235]U) [11]. To check the feasibility of rare earth hafnate RE$_2$Hf$_2$O$_7$ pyrochlores as ceramic hosts for incorporation of long-lived actinides, it is very essential to carry out speciation and structural studies on them, as it can have very strong influence on their behavior in the repository environment. In this context, carrying out speciation (e.g. oxidation state and coordination geometry) studies of uranium ion doped in RE$_2$Hf$_2$O$_7$ serves as a prerequisite for their capability for nuclear waste immobilization.

Uranium doped materials are also in high demand for other applications such as for space [12], laser [13], photocatalysis [14], nuclear

---
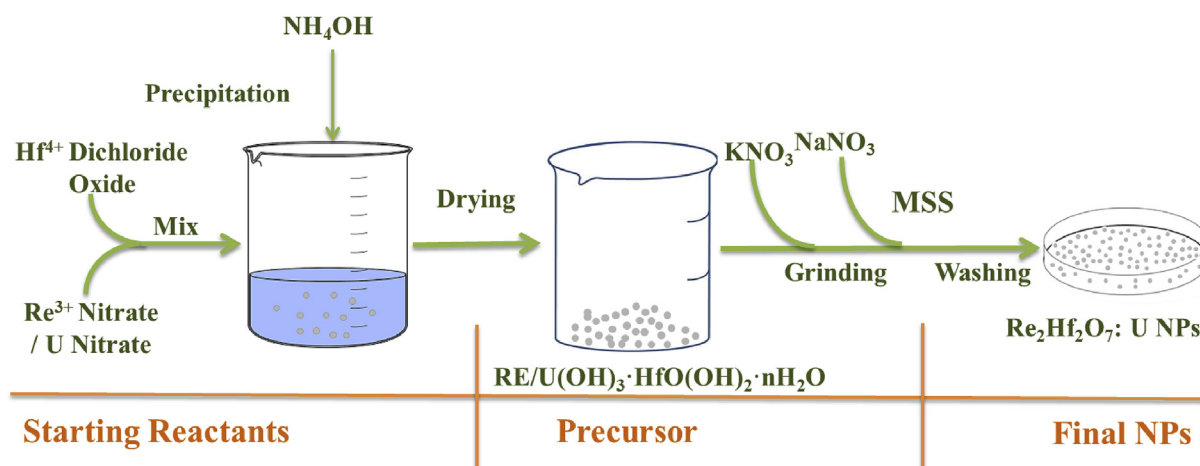
Scheme 1. Representative sketch for the synthesis of the RE$_2$Hf$_2$O$_7$:U NPs by molten salt synthesis.

fuel [15], and lithium ion batteries [16]. Uranium has highly enriching chemistry in doped inorganic compounds. It is known to display wide range of oxidation states ranging from +3 to +6, however +3 and +5 oxidation states are more likely to be stabilized in single crystals. In powdered compounds, its +4 and +6 oxidation states are the most prevalent states. Interestingly, the +6-oxidation state can exist either in the form of uranate ion UO$_6^{6-}$ or uranyl ion UO$_2^{2+}$ depending upon the host structure. The structure that favors metal single bond oxygen stabilizes uranium ion in the uranate form, whereas the structure that favors the formation of metal–oxygen double bond leads to the stabilization of the uranyl ion.

Photoluminescence is one of the most sensitive techniques for the speciation studies of uranium ions in doped compounds. This is mainly because each oxidation state of uranium ions has characteristic luminescence property and lifetime. Recently, a few research groups, including ours, have carried out some studies on uranium-doped zirconate pyrochlores, especially gadolinium zirconate [17–23]. For example, Kutty et al. studied phase stability as a function of doping level and oxidation state of uranium in Gd$_2$Zr$_2$O$_7$ using XPS [18]. Gregg and group suggested that uranium cation is largely located in the pyrochlore B-site instead of the targeted A-site in Gd$_2$Zr$_2$O$_7$:U along with the formation of cation antisite (A- and B-site mixing) disorder [19]. In addition, Gregg and group, also investigated the oxidation state of uranium in Gd$_2$Zr$_2$O$_7$:U samples after annealed in different environments [20]. On the other hand, Zhang and group investigated both the local site of uranium ion and pressure induced phase transition in Gd$_2$Zr$_2$O$_7$:U [21]. Finally, Lu et al. investigated the effects of U$_3$O$_8$ content on the phase and microstructure evolution of Gd$_2$Zr$_2$O$_7$ pyrochlore waste forms [22]. In our previous work, we investigated the effect of uranium speciation in La$_2$Hf$_2$O$_7$ pyrochlore host and found an extraordinary reversible phase transition between cotunnite and pyrochlore phases at 10% uranium doping level with changing temperature [24].

Because of their intrinsic small size and large surface area, nanoparticles (NPs) are expected to accommodate large concentration of actinide ions [24]. Moreover, it is assumed that NPs may exhibit high radiation stability and ease of forming antisite defects which are very important from nuclear waste host perspective [25].

The purpose of this work is to explore the potential of rare earth hafnate pyrochlores as hosts of actinide ions and the effect of change in the A-site on speciation of uranium ion in RE$_2$Hf$_2$O$_7$:U NPs, and to understand the uranium photochemistry and structure-optical properties correlation. In this context, we have synthesized various RE$_2$Hf$_2$O$_7$:U NPs wherein the A-site ions include Y^{3+}, Nd^{3+}, Gd^{3+} and Lu^{3+}. Their structural analysis was carried out using X-ray diffraction (XRD) and Raman spectroscopy. Moreover, time resolved

photoluminescence was used to decipher information related to oxidation state and coordination polyhedra. The phase stability of uranium in the RE$_2$Hf$_2$O$_7$:U NPs has been explored as well by doping various concentrations of uranium ion (1.0, 5.0 and 10.0%). Though the data reported here are preliminary, we will further characterize their structure using X-ray absorption spectroscopy and neutron diffraction.

2. Experimental

Four sets of uranium doped RE$_2$Hf$_2$O$_7$ (RE: Nd, Lu, Y, Gd) nanoparticles were obtained using the molten salts synthesis (MSS) [26,27]. Precursors for MSS were prepared via a co-precipitation route, where commercially available neodymium(III) nitrate hexahydrate (Nd(NO$_3$)$_3$·6H$_2$O, 99.9%), lutetium(III) nitrate hydrate (Lu(NO$_3$)$_3$·xH$_2$O, 99.999%), yttrium(III) nitrate hexahydrate (Y(NO$_3$)$_3$·6H$_2$O, 99.98%), gadolinium(III) nitrate hexahydrate (Gd(NO$_3$)$_3$·6H$_2$O, 99.9%), hafnium dichloride oxide octahydrate (HfCl$_2$O·8H$_2$O, 98%), and uranyl nitrate hexahydrate (UO$_2$(NO$_3$)$_2$·6H$_2$O, 98–102%) were used as reactants with no further purifications. Stoichiometric amounts of the starting reactants were calculated to obtain four different sets of the RE$_2$Hf$_2$O$_7$:U NPs doped with different concentrations of uranium (1.0, 5.0 and 10.0%). In all prepared samples, ratios were calculated so that uranium replaces a portion of A site cation of Nd, Lu, Y, or Gd. Measured reactants were dissolved in 200 ml of distilled water (18.2 MΩ at 25 °C), and titrated with 200 ml of ammonium hydroxide solution (10%, diluted from concentrated NH$_4$OH(aq, 28–30%) for a period of 2 h. The resulting precipitate was then washed several times with distilled water, vacuum filtrated, and dried at 90 °C overnight to obtain complex single-source precursors (1-x%)RE(OH)$_3$·x%U(OH)$_3$·HfO(OH)$_2$·nH$_2$O. The obtained precursor was then mixed with sodium nitrate (NaNO$_3$, 98%), and potassium nitrate (KNO$_3$, 99%) in a stoichiometric ratio of 1:30:30, and hand grinded for about 25 min. The resulted fine mixture was then annealed at 650 °C for 6 h with a ramp rate of 10 °C/min. The final product was washed with distilled water several times to get rid of any residual salts and dried at 90 °C overnight. The prepared samples are designated as YHO-Ux, NHO-Ux, GHO-Ux and LHO-Ux (x = 1, 5 and 10) for the uranium doped Y$_2$Hf$_2$O$_7$, Nd$_2$Hf$_2$O$_7$, Gd$_2$Hf$_2$O$_7$, and Lu$_2$Hf$_2$O$_7$ NPs, respectively. Scheme 1 shows a sketch of the synthesis of the RE$_2$Hf$_2$O$_7$:U NPs.

The obtained RE$_2$Hf$_2$O$_7$:U NPs were studied using several characterization techniques including XRD, Raman spectroscopy, scanning electron microscopy (SEM), and photoluminescence (PL) studies. To insure the phase purity of the RE$_2$Hf$_2$O$_7$:U NPs, XRD was carried out using a "BRUKER™ D8 X-ray Diffractometer" with a Cu K$_{\alpha 1}$ radiation (λ = 0.15406 nm, 40 kV, 40 mA). The scanning mode was set to 2θ, and the scanning range was from 10° to 90° with a scanning step size of
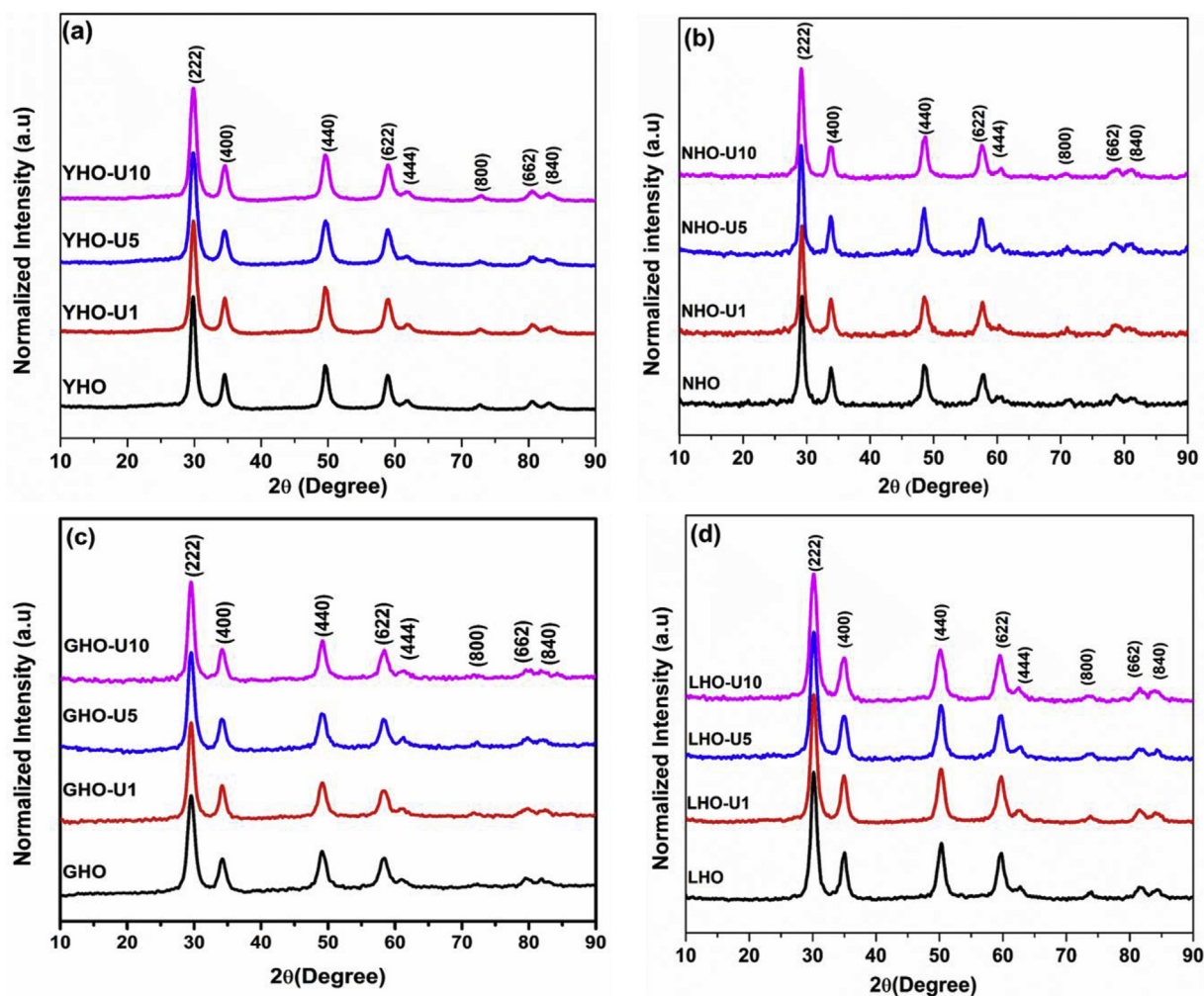
Fig. 1. XRD patterns of the $RE_2Hf_2O_7$:Ux (x = 0, 1, 5 and 10) NPs: (a) RE = Y, (b) RE = Nd, (c) RE = Gd, and (d) RE = Lu.

0.04° and scanning rate of 1.0° min^{-1}. Raman spectroscopy was used to study the phase and structure of the $RE_2Hf_2O_7$:U NPs and the effect of uranium doping on these properties. Raman spectra were collected with a Renishaw-2000 Raman spectrometer (Renishaw-2000, Renishaw, Inc.) with Ar laser (514 nm and 5 Mw). The microstructure and morphology of these NPs were studied using a Carl Zeiss sigma VP scanning electron microscopy (SEM) equipped with a field emission gun operated at 5 kV. To study the optical properties and assess the effect of doping on the optical properties, PL emission and excitation spectra were obtained with an Edinburgh Instrument FLS 980 fluorometer system equipped with a steady xenon lamp source.

3. Results and discussion

3.1. X-ray diffraction

Fig. 1a–d shows the XRD patterns of the $RE_2Hf_2O_7$:U NPs. All the samples display diffraction peaks of (222), (400), (440), (622), (444), (800), (662) and (840). However, this pattern is relatively close to that of the fluorite structure with peaks of (111), (200), (220), (311), (222), (400), (331) and (420). Those reflection peaks are contributed by both pyrochlore and fluorite structures. The weaker superlattice reflection peaks (111), (113) and (331) of ideal pyrochlore structure are not seen in the XRD patterns. It is well-known that $A_2B_2O_7$ pyrochlore oxide can stabilize in two different structures, ordered pyrochlore type with Fd$\bar{3}$m space group, and disordered fluorite type with Fm$\bar{3}$m space group. The sharp diffraction peaks for all the samples suggested the well-developed

$RE_2Hf_2O_7$ crystals. There is no diffraction pattern corresponding to oxides of rare earth ions, Hf or uranium, confirming the high purity of the synthesized NPs. From those patterns, it can also be seen that there is no change in the XRD on uranium doping, which indicates that uranium doping has not distorted the basic pyrochlore network. Moreover, the XRD patterns of YHO, NHO, GHO and LHO matches closely with the reported pattern of $Y_2Hf_2O_7$ [8], $Nd_2Hf_2O_7$ [5], $Gd_2Hf_2O_7$ [5] and $Lu_2Hf_2O_7$ [28]. Table 1 shows the lattice parameters and crystallite size of various $RE_2HF_2O_7$ NPs. It can be seen from this table that MSS can produce sub-10 nm particles for YHO, GHO and LHO. On the other hand, NHO NPs are on slightly higher side. Sub 10-nm particles are highly advantageous for biomedical applications where the material needs to travel in blood vessels and penetrate into cells [29].

3.2. Raman spectroscopy

XRD is often not able to distinguish the pyrochlore and fluorite structures because they only differ by an oxygen vacancy at 8b site. To confirm the structure of the $RE_2Hf_2O_7$:U NPs, vibrational analysis techniques are used. Especially, Raman spectroscopy is sensitive to the vibrational frequencies of the M−O bonds. Fig. 2a–d shows the Raman spectra of various undoped and U doped $RE_2Hf_2O_7$ (RE = Y, Nd, Gd and Lu) NPs. It is reported that ordered pyrochlore displays six distinct vibrational modes $A_{1g} + E_g + 4F_{2g}$ related to various metal-oxygen vibrations [7]. The first few modes at lower frequencies: F_{2g}, E_g, and F_{2g} modes, arise from vibrations of the A-O and B−O bonds, whereas the higher frequencies of F_{2g} arise from stretching of the B−O bonds. On the

Table 1
Lattice parameter and crystallite size of the $RE_2Hf_2O_7$:U NPs (RE = Y, Nd, Gd and Lu).

$Y_2Hf_2O_7$:x%U

Samples	2θ (∘)	FWHM (β)	Lattice parameter (Å)	Crystallite size (nm)
YHO	29.83	0.81	10.37	9.81 ± 0.261
YHO−U1	29.87	0.93	10.35	8.54 ± 0.279
YHO−U5	29.87	1.05	10.35	7.57 ± 0.297
YHO-10	29.87	0.97	10.35	8.19 ± 0.286
$Nd_2Hf_2O_7$:x%U				
NHO	29.26	0.72	10.56	11.03 ± 0.204
NHO−U1	29.25	0.70	10.57	11.35 ± 0.201
NHO−U5	29.16	0.62	10.60	12.81 ± 0.189
NHO-10	29.21	0.69	10.58	11.51 ± 0.199
$Gd_2Hf_2O_7$:x%U				
GHO	29.58	1.08	10.45	7.36 ± 0.277
GHO-U1	29.55	0.98	10.46	8.11 ± 0.264
GHO-U5	29.57	0.96	10.46	8.28 ± 0.261
GHO-10	29.54	0.84	10.47	9.46 ± 0.244
$Lu_2Hf_2O_7$:x%U				
LHO	30.20	0.97	10.24	8.19 ± 0.198
LHO-U1	30.19	0.97	10.25	8.19 ± 0.198
LHO-U5	30.18	1.05	10.25	7.57 ± 0.206
LHO-10	30.17	1.14	10.25	6.81 ± 0.217

other hand, disordered fluoride has just one broad band (F_{2g}) due to random distribution of 7 oxygen ions at 8-B-sites. The phase transition is highly sensitive to chemical doping, high temperature, irradiation and high pressure [30].

In addition to the fully ordered pyrochlore and completely disordered defect-fluorite, there is also increasing evidence for partial order/disorder structure of $A_2B_2O_7$ compounds [31]. Any disorder, such as vacancies, interstitials, and structural defects, may destroy the translational periodicity of the lattice. This leads to phonons from all parts of the Brillouin zone to start contributing to the optical spectra, thereby giving rise to broadened, continuously spread, and weak-intensity bands [32]. Other than pyrochlore and fluorite phases, $A_2B_2O_7$ type compounds can also exist in another disordered phase known as cotunnite under high pressure [33].

Undoped YHO has Raman peaks around 323, 384, 464 and 554 cm^{-1} submerged over a very broad peak. Moreover, all these peaks are highly broad in nature, which suggested the absence of characteristics pyrochlore sextet. Therefore, YHO does not exist in ideal pyrochlore (IP) nor pure disordered fluorite (DF) structure, but in what can be called a delta pyrochlore structure (DPS). DPS is less ordering than IP but more than DF. The same structure persists until 1.0% uranium doping, but at higher doping YHO−U stabilizes in highly disordered cotunnite phase. The broad mode between 700 and 800 cm^{-1} is not a fundamental Raman mode in pyrochlore-structured oxides, and is believed to be due to distortions to the BO_6 octahedra [34]. Based on the Raman spectra, the YHO NPs have delta pyrochlore structure, the
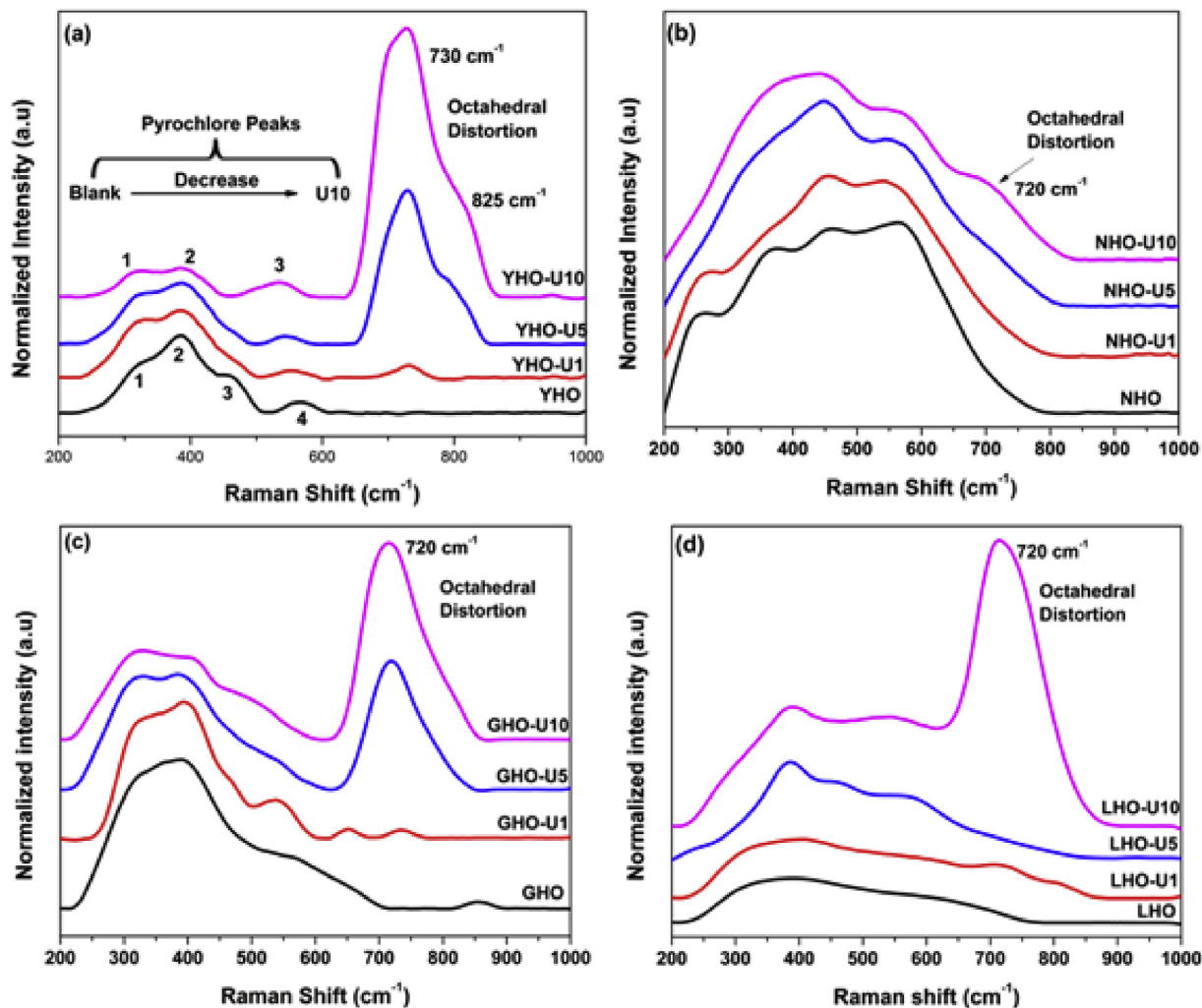

Fig. 2. Raman spectra of the $RE_2Hf_2O_7$:U NPs: (a) RE = Y, (b) RE = Nd, (c) RE = Gd, and (d) RE = Lu.

YHO−U1 NPs have disordered fluorite structure, while the YHO−U5 and YHO−U10 NPs have cotunnite structure.

On the other hand, the NHO NPs have more resolved peaks in the 200-600 cm^{-1} region, specifically around 221, 254, 367, 454, 521 and 575 cm^{-1}. The peak at 221 cm^{-1} is a signature of HfO_6 distortion whereas that at 521 cm^{-1} is attributed to A_{1g}/F_{2g}. Although there are few vibrational modes corresponding to ideal pyrochlore, they are more like intermediate DPS. The extent of disordering seems to increase as a function of uranium doping and at higher uranium doping of 5.0 mol% and 10.0 mol% the structure seems to consist of single broad peak. It looks more like a disordered fluorite at 10.0% uranium doping.

When we switch over to GHO, there is a single broad peak which is clear signature of disordered fluorite structure and it remains the same with 1.0% uranium doping while, at 5.0% and 10.0% uranium doping there is a phase transition from disordered fluorite (Fm-3m) to orthorhombic cotunnite phase (Pnma). Normally, it is reported that fluorite-structured oxides typically transform to cotunnite at high pressure [35].

Lutetium hafnium oxide also display very interesting structural behavior. For the LHO and LHO-U1 samples, Raman spectra consist of a single broad Raman band typical of defect fluorite structure. At intermediate composition, some ordering is induced and there is evolution of ideal pyrochlore structure but again it is transformed to disordered cotunnite at 10% doping.

To sum, $Y_2Hf_2O_7$ was found to exist in slightly disordered pyrochlore structure designated as delta pyrochlore phase and the extent of disordering increases as a function of uranium doping while the structure reaches a cotunnite phase at 10.0% doping level. $Nd_2Hf_2O_7$ also exists in a distorted pyrochlore structure and its distortion increases with increasing uranium doping while the phase transforms into a disordered fluorite structure at 10.0% uranium doping. Both $Gd_2Hf_2O_7$ and $Lu_2Hf_2O_7$ samples exist in a disordered fluorite structure and transforms into cotunnite structure at high U concentrations. It is seen from the Raman spectroscopy that higher uranium concentration increases the extent of disordering. This is obvious due to increase in disordering induced by charge and size matching as uranium ions enter the $A_2B_2O_7$ lattice. Uranium ions occupying the A and B sites need to be compensated by large amount of cation vacancies. As reported in our early work based on positron annihilation lifetime spectroscopy, U doping in pyrochlore network creates large amount of cation vacancies [23]. Such defects near the $A_2B_2O_7$ lattice sites create distortion of the basic pyrohafnate network.

3.3. Morphological study

Representative SEM images of the $RE_2Hf_2O_7$:U1 NPs (RE = Y, Nd, Gd and Lu) (Fig. 3) show that these NPs are spherical, highly monodispersed and uniform in nature with average sizes in the range of 25–45 nm. The particle sizes estimated from SEM images are larger than the crystallite sizes calculated from XRD data, which indicates that each particle is composed of a few crystallite grains.

3.4. Photoluminescence spectroscopy

Fig. 4a shows the excitation spectra of the YHO-Ux NPs. The YHO−U1 NPs display a broadband peaking around 270 nm. This is ascribed to ligand to metal charge transfer that involves electronic transition from filled O 2p orbital to partially filled U 5f orbital. In this case, it is assigned to charge transfer transitions within the octahedral UO_6^{6-} group [36]. Interestingly this particular band exhibits red shift to 290 nm at higher uranium doping (5 and 10%). This can be explained by lattice strain induced in the YHO NPs at higher uranium doping levels which may reduce the band gap. Similar observation was also made in Sb^{3+} doped glasses by Xu et al. [37] On the other hand, emission spectra of the YHO−U1 NPs (Fig. 4b) shows a broadband green luminescence at around 540 nm. This is attributed to uranium in

+6 oxidation state in the form of octahedral uranate ion UO_6^{6-}. The coordination number of hexavalent uranium in oxides seems to be an important factor that determines the luminescence properties of uranium-activated oxides. Blasse and gorup, has ascribed red uranium emission to tetrahedral uranate, and green emission to octahedral uranate [38]. Runciman and his group, way back in 1955, have ascribed for the first time green uranium luminescence to the presence of UO_6^{6-} groups [39]. This is similar to what has been reported earlier in $SrZrO_3$, and $Nd_2Zr_2O_7$ [17,40]. The emitting centre in this type of compounds occupies a site with inversion symmetry. This is attributed to the fact that YHO favors the stabilization of uranium single bond oxygen (U−O). The luminescence intensity of YHO−U decreases at higher uranium doping because of conventional concentration quenching process. For higher uranium content, concentration quenching of the uranium emission occurs due to radiationless lost by energy transfer between uranate centers, followed by transfer to killer sites. The emission band of YHO−U1 shows the obvious asymmetric shapes, indicating the existence of two different luminescent centers [41]. This can be attributed to distribution of uranate ion at both YO_8 (ideal cube) and HfO_6 (distorted octahedral).

In the structure of YHO, there are two non-equivalent sites as Y^{3+} and Hf^{4+}. Y ions are surrounded by eight oxygen ions in a symmetrical cube geometry. While the Hf^{4+} ions, on the other hand, are surrounded by six oxygen atoms in the form of distorted octahedral geometry. The Hf site is more distorted than that of Y. In addition, the bond-length of Hf−O is shorter than that of Y−O. Thus, in YHO−U1, the high-energy emission at 490 nm (U_B) originates from the uranate ions which occupy loose crystal circumstance with longer Y−O bonds (Y site), and the low-energy emission at 540 nm (U_G site) is ascribed to the uranate ions occupying compact crystal circumstance with shorter Hf–O bond length (Hf site). Interestingly, the emission shifts to higher wavelength in orange region (~ 590 nm) at higher uranium doping. From Raman spectroscopy, we have seen that at higher uranium concentrations, structure of YHO changes from DPS to cotunnite. The cotunnite structure has relatively higher structural disordering than fluorite. This is what is reflected in emission spectra at higher uranium doping wherein green maxima shifts to orange maxima due to structural phase transition from DPS to cotunnite structure.

In case of the NHO-Ux NPs (Fig. 5a), which exist in DPS phase for NHO and NHO−U1 and DF for NHO−U5 and NHO−U10, excitation spectra displayed a broad band around 307 nm that is again ascribed to intrinsic oxygen to uranium charge transfer band. As a function of uranium concentration, there is not much change in the band position; though slight variation in intensity of charge transfer band is seen. Interestingly, the emission spectra shown in Fig. 5b displayed a broad band in the blue region around 485 nm due to emission from octahedral uranate ion. As discussed earlier NHO and NHO−U1 has more ordered structure, though not ideal pyrochlore but more ordered than fluorite structure. Here, uranate ion stabilizes only at A-site that is NdO_8 polyhedra as there is no signature of uranate emission in green/orange region. However, there are smaller kinks around 635 and 715 nm ascribed to presence of defects in NHO−U. These are attributed to localization of U^{6+} only at Nd^{3+} site which leads to creation of charge compensating defects. Unlike in YHO, where the defect density arises because charge compensation will be relatively less as U^{6+} is distributed at both Y^{3+} and Hf^{4+} sites.

In case of $Gd_2Hf_2O_7$, which has pure disordered fluorite structure for GHO and GHO-U1 and cotunnite for GHO-U5 and GHO-U10, excitation spectra (Fig. 6a) displayed similar characteristics featuring charge transfer transition around 290 nm with different intensities at different uranium doping. Fig. 6b shows the emission spectra of GHO-U for different doping concentrations. Although, uranium stabilizes as +6 oxidation state in our GHO-U NPs, interestingly, it does it in the form of uranyl ion (UO_2^{2+}) instead of octahedral uranate (UO_6^{6-}). This is because uranium ions exist as U=O with shorter bond length (> 1.8 Å). In both cases, the emission arises due to ligand to metal charge transfer
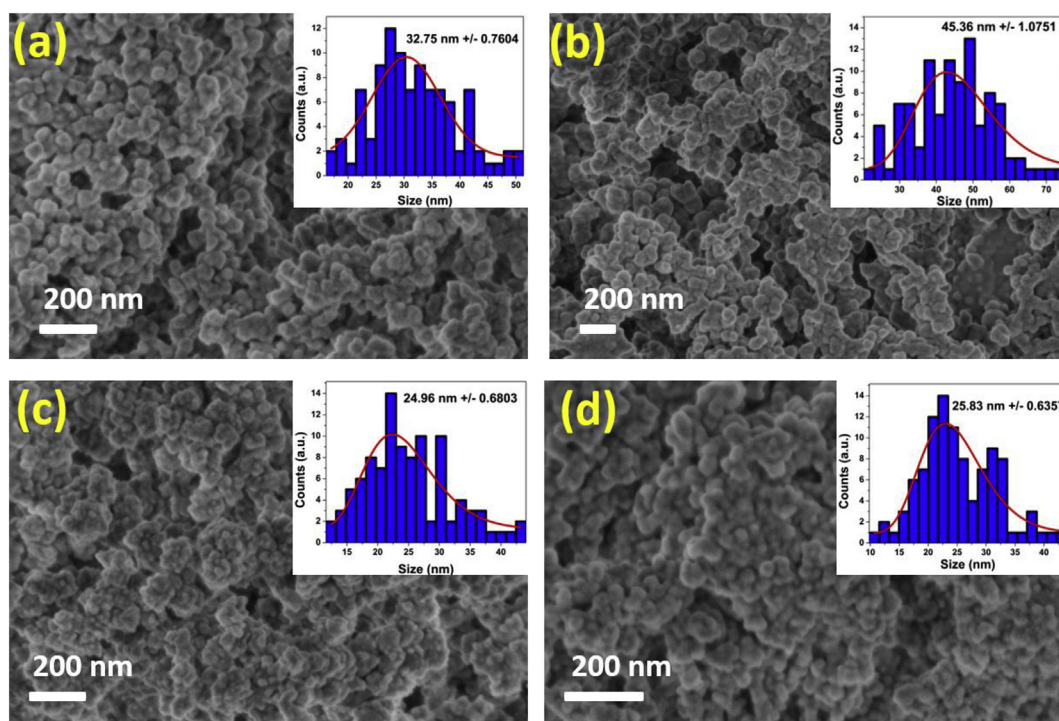
Fig. 3. Representative SEM images of (a) YHO−U1, (b) NHO−U1, (c) GHO-U1 and (d) LHO-U1 NPs. Insets are particle size histograms derived using ImageJ software.

involving bonding oxygen orbitals (Πu, Πg, Ωg, Ωu) to nonbonding $5f_\delta$ and $5f_\Phi$ orbitals of uranium. UO_2^{2+} has a closed shell singlet ground state with 12 valence electrons (originating in the oxygen 2p and uranium 5f, 6d and 7s AOs). The resulting bonding combinations are fully occupied in the ground state, accommodating 12 valence electrons, while the corresponding anti-bonding combinations are empty.

Lutetium hafnate also displayed very interesting structural behavior. Undoped and LHO-U1 consist of single broad Raman band typical of defect fluorite structure. At intermediate composition, some ordering is induced and there is evolution of ideal pyrochlore structure but again it is transformed to disordered cotunnite at 10% doping. In case of LHO-U, structurally we have seen there is anomalous trend in Raman spectra. LHO-U1 was having DF structure whereas LHO-U10 exist in cotunnite phase. However, intermediate composition of LHO-U5 has structure more close to pyrochlore phase. In excitation spectra shown in Fig. 7a

for LHO-U, there is a charge transfer band around 290 nm at 1.0% U that shifted to 340 nm at higher doping levels similar to what we have seen in case of YHO−U. Interestingly in emission spectra (Fig. 7b) for LHO-U1 there is a broad band at around 539 corresponding to octahedral uranate ion. However, there is progressive shift in this band at higher uranium doping to 565 nm for LHO-U5 and to 589 nm for LHO-U10. Such spectral shift in emission band is attributed to tunneling of uranate ion from LuO_8 to HfO_6 at higher uranium concentrations.

4. Discussion

The reason for phase transition to more distorted cotunnite structure on higher uranium doping is attributed to creation of charge compensating defect as a result of aliovalent doping of hexavalent uranium at trivalent RE or tetravalent hafnium sites. In all probabilities,
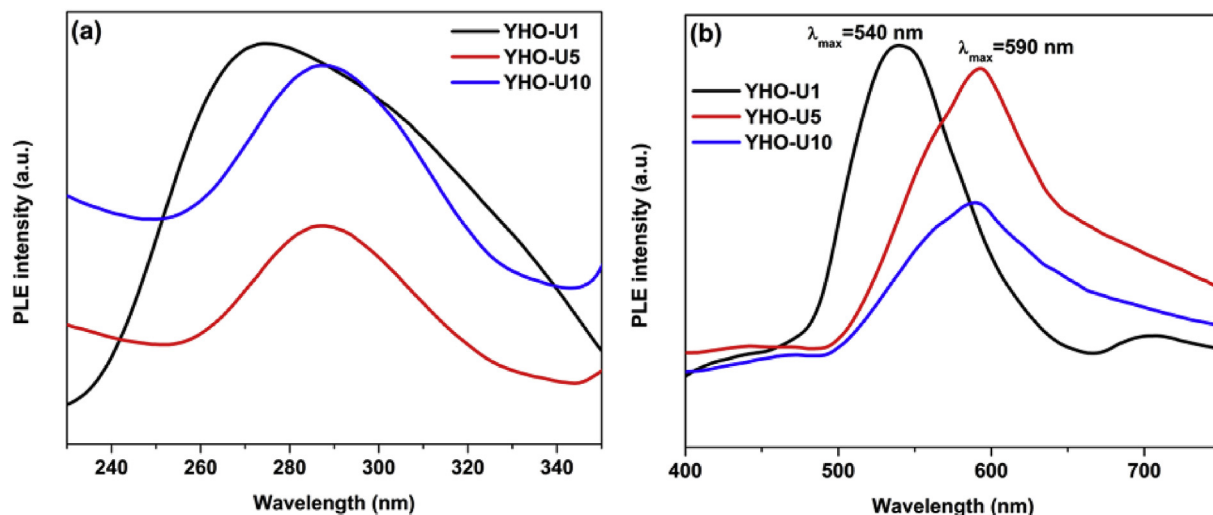

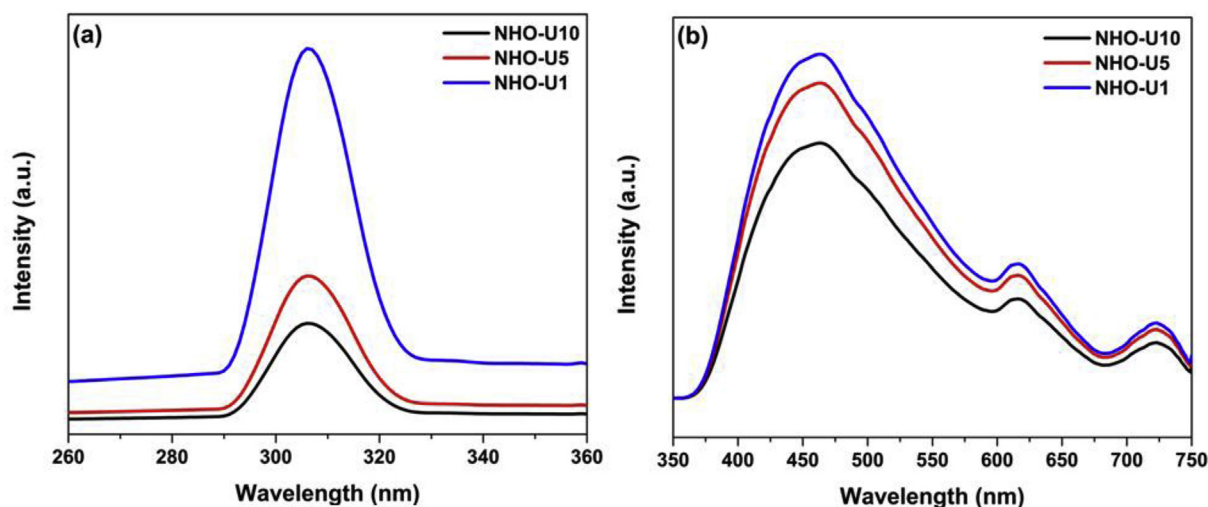**Fig. 4.** (a) Excitation and (b) emission spectra of the YHO-Ux (x = 1, 5 and 10) NPs.

Fig. 5. (a) Excitation and (b) emission spectra of the NHO-Ux (x = 1, 5 and 10) NPs.

the higher fraction of uranium will occupy REO$_8$ polyhedra due to closeness of 5f uranium ion with 4f rare earth ion. Uranium incorporation at RE site will certainly cause severe distortion in the basic network by creating negatively charged rare earth ion vacancy. Heavier actinide such as uranium ion has strong affinity towards electron cloud distortion because of increased polarizability and thus distorted cotunnite or fluorite structure. This may be the plausible cause of transformation to cotunnite or fluorite structure. The phase that forms in each case depends of the degree of distortion caused by uranium doping. The degree of distortion created in each case is also governed by f-f electron interaction of uranium and rare earth ion. Y^{3+} (4f^0, no f electron), Gd^{3+} (4f^7, half-filled stability) and Lu^{3+} (f^{14}, full-filled stability) may exhibit similar interaction with uranium ions, unlike Nd^{3+} (4f^3, partial filled) which may have a different kind of interaction with uranium ions. Consistent with the Raman spectra and the observed PL data, this may be the reason that the YHO−U, GHO-U and LHO-U NPs are stabilized in cotunnite structure and the NHO−U NPs are stabilized in fluorite structure at high uranium doping level. Our previous work on La$_2$Hf$_2$O$_7$:U NPs, shows very interesting structural transitions: low uranium doping concentrations favor ideal pyrochlore, intermediate uranium doping concentrations have mixed pyrochlore and cotunnite phases, whereas and uranium doping concentrations at 7.5% and higher possess cotunnite structure as the most stable phase [24]. Furthermore, for the YHO, GHO and LHO NPs, the Raman spectra of the

undoped, 1.0% doped, and 10% doped samples all have similar features for each case. The only difference is the appearance of cotunnite disordering at different uranium doping levels for these hosts: 5.0% in the LHO NPs whereas 10% in the YHO and GHO NPs. This may be due to the presence of paired f-shell electrons for Lu^{3+} unlike none for Y^{3+} or Gd^{3+} ions. However, further studies are necessary to prove this phenomenon, e.g. neutron diffraction analysis, in the future.

Uranyl ions are characterized by uranium-oxygen partial triple bond character whereas octahedral uranate ions are characterized by uranium-oxygen single bond. Crystal lattice which favors the formation of U−O bond stabilizes uranium ion the form of UO$_6^{6-}$ ion. In comparison, crystal lattice which offers much closer packed environment and favors shorter triply bonded uranium-oxygen bond tends to stabilize uranium in the form of UO$_2^{2+}$ ion. In the Gd$_2$Hf$_2$O$_7$ NPs, uranium stabilizes as uranyl ion. This interesting behavior may imply that U=O is the favorable way that uranium is localized in the Gd$_2$Hf$_2$O$_7$ NPs. On the other three hafnate NPs, the U−O single bond is the energetically favorable species. In both cases of the uranium ions, the emissions arise from ligand to metal charge transfer involving bonding oxygen orbital (Πu, Πg, Ωg, Ωu) to non-bonding 5f$_\delta$ and 5f$_\Phi$ orbitals of uranium. The signature of uranyl ion is vibronic progression with constant spacing. Such uniformly distributed vibrational progression arises from strong interaction of the ground state Raman active O=U=O symmetric stretching mode with the ^{3}Π$_u$ electronic triplet excited state (generally
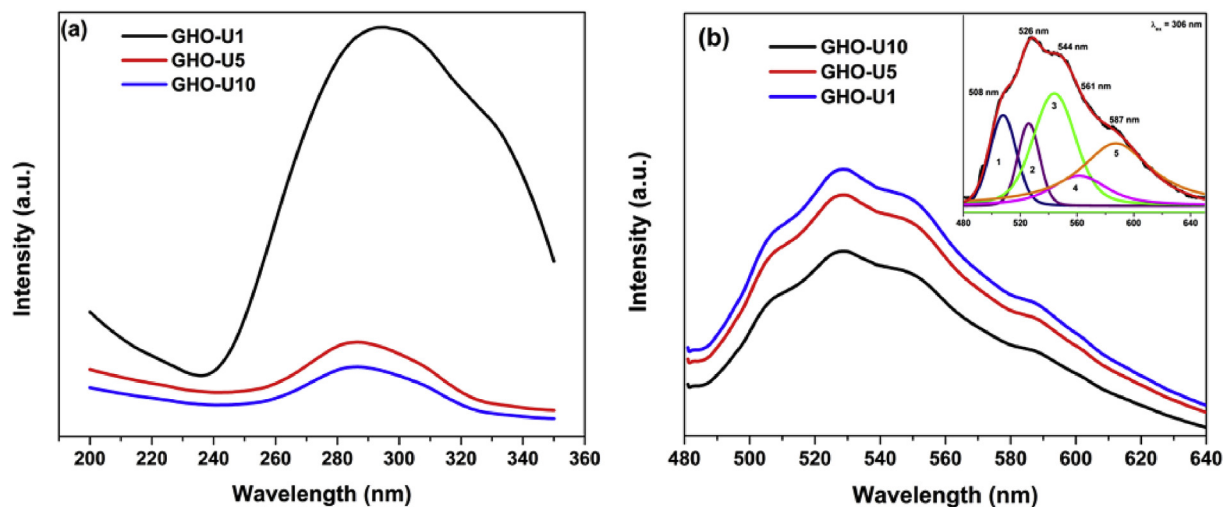

Fig. 6. (a) Excitation and (b) emission spectra of the GHO-Ux (x = 1, 5 and 10) NPs.
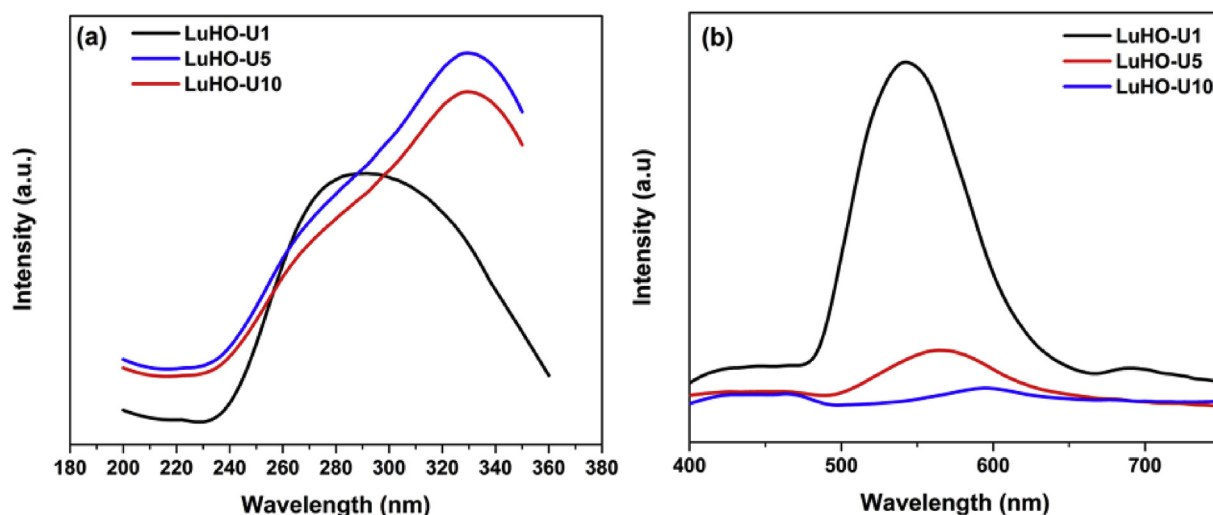
Fig. 7. (a) Excitation and (b) emission spectra of the LHO-Ux (x = 1, 5 and 10) NPs.

observed between 780 and 900 cm^{-1}).

The energy level diagram for uranyl ion has been displayed in Fig. 8. These valence electrons are accommodated in four MOs, transforming as π_g, π_u, σ_g and σ_u in the $D_{\infty h}$ molecular point group, and the centrosymmetric nature of this point group neatly separates the contributions to these MOs of the uranium 6d (g) and 5f (u) AOs [42]. The lowest excited states originate from transitions out of the bonding σ_u orbital into the nonbonding δu or Φu orbitals. When the Coulomb electrostatic and exchange interactions between the two electrons (in δu and Φu orbitals, respectively) and the spin–orbit coupling are taken into account, the low-lying excited states further split into 8 excited states [43,44]. As seen from the inset of Fig. 6b, the emission spectra displayed five band peaking around 508, 526, 544, 561 and 587 nm. For axial $[O=U=O]^{2+}$ structure, three Raman active vibrational modes exist symmetric and asymmetric U−O stretching modes (ν_s and ν_{as}) and the O−U−O bending mode (ν_b). The fact that 5f orbitals are

non-bonding in nature, the U−O bond length is expected to increase in excited state [45]. As a result, the ν_s in excited state should be less than that in the ground state. As per Franck Condon (FC) principle, only ν_s can couple to electric dipole transitions (EDT) in the UO_2^{2+} ion [46]. Therefore, as a notable characteristic of uranyl spectra, including absorption and emission, vibronic bands progress harmonically up to six orders in the symmetric stretching modes.

The position of first vibrational band (ν_{0-0}) is most confirmatory signature in deciding the number of oxygen ions around uranium and bond order of U−O which is normally termed as zero phonon band (ZPB) [43,44]. ZPB for UO_2^{2+} can vary from 440 to 520 nm and the fact that in our spectrum it is observed at 508 and the subsequent vibrational progression can be seen at room temperature is an indication that U(+6) stabilizes as UO_2^{2+} in GHO. In case of YHO and NHO, such vibronic coupling to Raman active symmetric stretching is not possible, so their spectra collapse as a broad band characteristic of charge
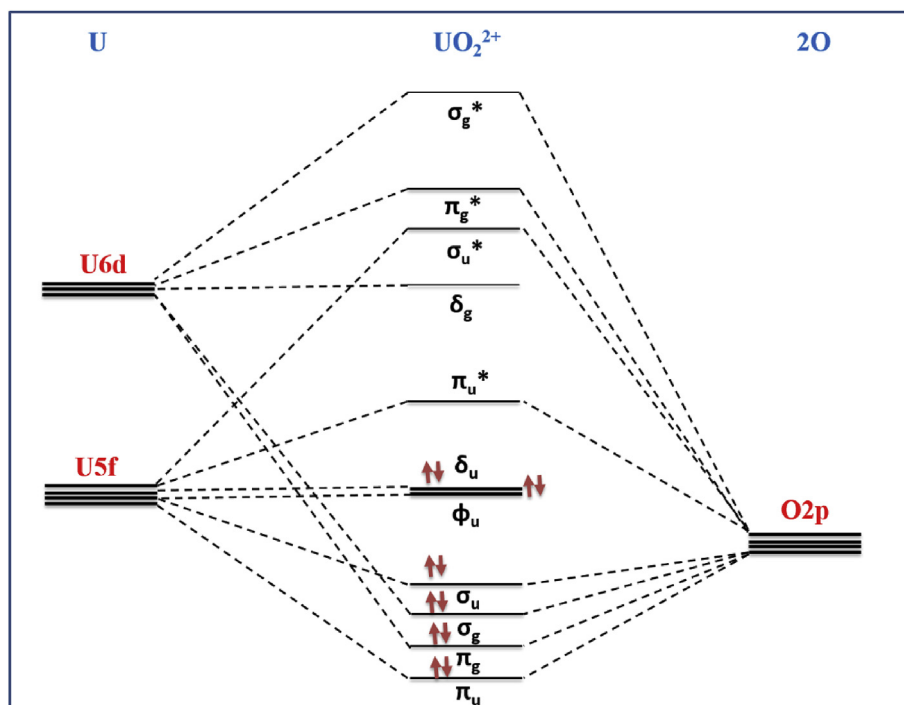

Fig. 8. Qualitative energy level diagram of UO_2^{2+} [47].

transfer transition.

5. Conclusion

In this work, we have synthesized several RE$_2$Hf$_2$O$_7$ matrices (RE = Y, Gd, Nd, and Lu) doped at different concentrations of uranium (x = 0, 1, 5, and 10). The main purpose is to address and compare the adaptability difference of uranium ions in these hosts by exploring their structural and optical properties. All these samples are in the nanosized domain. Phase transition from delta pyrochlore to disordered fluoride to orthorhombic cotunnite phase occurs with uranium doping. Emission intensities decrease with the increase of uranium concentration due to concentration quenching. In the case of YHOU, the green luminescence was attributed to +6 oxidation state in the form of octahedral uranate UO$_6^{6-}$ with a shift to orange maxima due to structural phase transition from DFS to cotunnite structure. Optical characteristics of NHOU and LHOU also shown stabilization of uranate UO$_6^{6-}$ ion. On the other hand, GHOU matrices stabilized uranium as +6 oxidation state but in the form of uranyl ion (UO$_2^{2+}$) due to U=O with shorter bond length. The coordination number in which the uranium ion stabilized in each of the matrices determined the luminescent profiles and such comparisons are important. The novelty of this work is the comparison of uranium in different matrices involving phase transformation induced by chemical doping and correlating optical modification to structural rearrangement. Such investigations are of great significance in fundamental solid-state spectroscopy of uranium and paramount in nuclear waste immobilization.

References

[1] S. Gu, S. Zhang, B. Xue, J. Yan, W. Li, L. Zhang, Phase variation and thermophysical properties of La$_2$Hf$_2$O$_7$ with alumina addition, J. Eur. Ceram. Soc. 38 (2018) 1938–1945.
[2] V.A. Vorozhtcov, V.L. Stolyarova, S.I. Lopatin, E.P. Simonenko, N.P. Simonenko, K.A. Sakharov, V.G. Sevastyanov, N.T. Kuznetsov, Vaporization and thermodynamic properties of lanthanum hafnate, J. Alloy. Comp. 735 (2018) 2348–2355.
[3] S. Gu, S. Zhang, D. Xu, W. Li, J. Yan, Evolution of microstructure and hot corrosion performance of La$_2$Hf$_2$O$_7$ ceramic in contact with molten sulfate-vanadate salt, Ceram. Int. 44 (2018) 2048–2057.
[4] M. Sun, B. Huang, Comparison and correlation of structural disorder caused by anion Frenkel in affecting ion conduction of La$_2$Hf$_2$O$_7$ and La$_2$Mo$_2$O$_9$ as high performance electrolytes in SOFCs, MRS Adv. 2 (2017) 3317–3322.
[5] V.G. Sevastyanov, E.P. Simonenko, N.P. Simonenko, V.L. Stolyarova, S.I. Lopatin, N.T. Kuznetsov, Synthesis, vaporization and thermodynamic properties of superfine Nd$_2$Hf$_2$O$_7$ and Gd$_2$Hf$_2$O$_7$, Eur. J. Inorg. Chem. 2013 (2013) 4636–4644.
[6] X. Cheng, Z. Qi, G. Zhang, Y. Chen, T. Li, G. Pan, M. Yin, The interface reaction of high-k La$_2$Hf$_2$O$_7$/Si thin film grown by pulsed laser deposition, Appl. Surf. Sci. 256 (2009) 838–841.
[7] J.P. Zuniga, S.K. Gupta, M. Pokhrel, Y. Mao, Exploring the optical properties of La$_2$Hf$_2$O$_7$:Pr^{3+} nanoparticles under UV and X-ray excitation for potential lighting and scintillating applications, New J. Chem. 42 (2018) 9381–9392.
[8] G. Zhou, Z. Wang, B. Zhou, Y. Zhao, G. Zhang, S. Wang, Fabrication of transparent Y$_2$Hf$_2$O$_7$ ceramics via vacuum sintering, Opt. Mater. 35 (2013) 774–777.
[9] J. Papan, D.J. Jovanović, K. Vuković, K. Smits, V. Đorđević, M. Dramićanin, Europium (III)-doped A$_2$Hf$_2$O$_7$ (A = Y, Gd, Lu) nanoparticles: Influence of annealing temperature, europium (III) concentration and host cation on the luminescent properties, Opt. Mater. 61 (2016) 68–76.
[10] N. Cepeda-Sánchez, A. Fuentes, F. López-Cota, M. Rodríguez-Reyes, J. Díaz-Guillén, Mechanochemical synthesis and electrical properties of Gd$_2$Hf$_{2-x}$Zr$_x$O$_7$ solid

[11] electrolytes for their use in SOFC's, J. Appl. Electrochem. 45 (2015) 1231–1237.
[11] H. Xu, Y. Wang, P. Zhao, W.L. Bourcier, R. Van Konynenburg, H.F. Shaw, Investigation of pyrochlore-based U-bearing ceramic nuclear waste: Uranium leaching test and TEM observation, Environ. Sci. Technol. 38 (2004) 1480–1486.
[12] J.-f.o. Vigier, D. Freis, P. Pöml, D. Prieur, P. Lajarge, S.b. Gardeur, A. Guiot, D. Bouëxière, R.J. Konings, Optimization of uranium-doped Americium oxide synthesis for space application, Inorg. Chem. 57 (2018) 4317–4327.
[13] Q. Zhang, T. Lu, N. Wei, X. Chen, Z. Lu, L. Chen, J. Qi, Z. Huang, T. Hua, S. Wang, Synthesis of pure-phase uranium-doped YAG powder via co-precipitation method, Mater. Lett. 188 (2017) 396–398.
[14] Y. Liu, B. Becker, B. Burdine, G.E. Sigmon, P.C. Burns, Photocatalytic decomposition of Rhodamine B on uranium-doped mesoporous titanium dioxide, RSC Adv. 7 (34) (2017) 21273–21280.
[15] A. Shields, S. Ruiz-Hernandez, N. De Leeuw, Configurational analysis of uranium-doped thorium dioxide, IOP Conference Series: Materials Science and Engineering, IOP Publishing, 2015, p. 012007.
[16] F.G. El-Metwaly, M.M. Abou-Sekkina, F.A. Saad, A.M. Khedr, Synthesis, effect of γ-ray and electrical conductivity of uranium doped nano LiMn$_2$O$_4$ spinels for applications as positive electrodes in Li-ion rechargeable batteries, Mater. Sci. Poland 32 (2014) 571–577.
[17] S.K. Gupta, C. Reghukumar, M. Keskar, R. Kadam, Revealing the oxidation number and local coordination of uranium in Nd$_2$Zr$_2$O$_7$ pyrochlore: A photoluminescence study, J. Lumin. 177 (2016) 166–171.
[18] K.G. Kutty, R. Asuvathraman, R.R. Madhavan, H. Jena, Actinide immobilization in crystalline matrix: a study of uranium incorporation in gadolinium zirconate, J. Phys. Chem. Solid. 66 (2–4) (2005) 596–601.
[19] D.J. Gregg, Z. Zhang, G.J. Thorogood, B.J. Kennedy, J.A. Kimpton, G.J. Griffiths, P.R. Guagliardo, G.R. Lumpkin, E.R. Vance, Cation antisite disorder in uranium-doped gadolinium zirconate pyrochlores, J. Nucl. Mater. 452 (2014) 474–478.
[20] D.J. Gregg, Y. Zhang, Z. Zhang, I. Karatchevtseva, M.G. Blackford, G. Triani, G.R. Lumpkin, E.R. Vance, Crystal chemistry and structures of uranium-doped gadolinium zirconates, J. Nucl. Mater. 438 (2013) 144–153.
[21] F. Zhang, M. Lang, C. Tracy, R.C. Ewing, D.J. Gregg, G. Lumpkin, Incorporation of uranium in pyrochlore oxides and pressure-induced phase transitions, J. Solid State Chem. 219 (2014) 49–54.
[22] X. Lu, C. Hou, Y. Xie, X. Shu, Y. Ding, D. Ma, W. Ren, L. Bian, High capacity immobilization of U$_3$O$_8$ in Gd$_2$Zr$_2$O$_7$ ceramics via appropriate occupation designs, Ceram. Int. 43 (2017) 3015–3024.
[23] S.K. Gupta, C. Reghukumar, N. Pathak, K. Sudarshan, D. Tyagi, M. Mohapatra, P.K. Pujari, R.M. Kadam, Speciation of uranium and doping induced defects in Gd$_{1.98}$U$_{0.02}$Zr$_2$O$_7$: Photoluminescence, X-ray photoelectron and positron annihilation lifetime spectroscopy, Chem. Phys. Lett. 669 (2017) 245–250.
[24] M. Abdou, S.K. Gupta, J.P. Zuniga, Y. Mao, On structure and phase transformation of uranium doped La$_2$Hf$_2$O$_7$ nanoparticles as an efficient nuclear waste host, Mater. Chem. Front. 2 (2018) 2201–2211.
[25] W.-Q. Shi, L.-Y. Yuan, Z.-J. Li, J.-H. Lan, Y.-L. Zhao, Z.-F. Chai, Nanomaterials and nanotechnologies in nuclear energy chemistry, Radiochim. Acta 100 (8–9) (2012) 727–736.
[26] Y. Mao, X. Guo, J.Y. Huang, K.L. Wang, J.P. Chang, Luminescent nanocrystals with A$_2$B$_2$O$_7$ composition synthesized by a kinetically modified molten salt method, J. Phys. Chem. C 113 (2009) 1204–1208.
[27] Y. Mao, T.J. Park, F. Zhang, H. Zhou, S.S. Wong, Environmentally friendly methodologies of nanostructure synthesis, Small 3 (2007) 1122–1139.
[28] L. An, A. Ito, T. Goto, Fabrication of transparent Lu$_2$Hf$_2$O$_7$ by reactive spark plasma sintering, Opt. Mater. 35 (2013) 817–819.
[29] W. Jiang, B.Y. Kim, J.T. Rutka, W.C. Chan, Nanoparticle-mediated cellular response is size-dependent, Nat. Nanotechnol. 3 (2008) 145.
[30] K.M. Turner, D.R. Rittman, R.A. Heymach, C.L. Tracy, M.L. Turner, A.F. Fuentes, W.L. Mao, R.C. Ewing, Pressure-induced structural modifications of rare-earth hafnate pyrochlore, J. Phys. Condens. Matter 29 (2017) 255401.
[31] Z. Zhang, S.C. Middleburgh, M. de los Reyes, G.R. Lumpkin, B.J. Kennedy, P.E. Blanchard, E. Reynolds, L.-Y. Jang, Gradual structural evolution from pyrochlore to defect-fluorite in Y$_2$Sn$_{2-x}$Zr$_x$O$_7$: Average vs local structure, J. Phys. Chem. C 117 (2013) 26740–26749.
[32] R. Rejith, J.K. Thomas, S. Solomon, Structural, optical and impedance spectroscopic characterizations of RE$_2$Zr$_2$O$_7$ (RE = La, Y) ceramics, Solid State Ionics 323 (2018) 112–122.
[33] F. Zhang, J. Wang, J. Lian, M. Lang, U. Becker, R. Ewing, Phase stability and pressure dependence of defect formation in Gd$_2$Ti$_2$O$_7$ and Gd$_2$Zr$_2$O$_7$ pyrochlores, Phys. Rev. Lett. 100 (2008) 045503.
[34] D.R. Rittman, K.M. Turner, S. Park, A.F. Fuentes, C. Park, R.C. Ewing, W.L. Mao, Strain engineered pyrochlore at high pressure, Sci. Rep. 7 (2017) 2236.
[35] D.R. Rittman, K.M. Turner, S. Park, A.F. Fuentes, J. Yan, R.C. Ewing, W.L. Mao, High-pressure behavior of A$_2$B$_2$O$_7$ pyrochlore (A = Eu, Dy; B = Ti, Zr), J. Appl. Phys. 121 (2017) 045902.
[36] D. Taikar, C. Joshi, S. Moharil, SrO:U^{6+} green light emitting phosphor, J. Lumin. 153 (2014) 304–306.
[37] D. Xu, R. Wei, J. Cao, H. Guo, Luminescence and energy transfer of Sb^{3+}/Dy^{3+} co-doped magnesium sodium-phosphate glasses, Opt. Mater. Express 7 (2017) 2899–2904.
[38] J.T.W. De Hair, G. Blasse, Luminescence of the octahedral uranate group, J. Lumin. (5–6) (1976) 307–323.
[39] W. Runciman, Atomic configurations in luminescent centres, Br. J. Appl. Phys. 6 (1955) S78.
[40] S.K. Gupta, N. Pathak, R. Gupta, S. Thulasidas, V. Natarajan, Probing the oxidation state and coordination geometry of uranium ion in SrZrO$_3$ perovskite, J. Mol.

Struct. 1068 (2014) 204–209.

[41] J. Gan, Y. Huang, L. Shi, X. Qiao, H.J. Seo, Luminescence properties of Eu^{2+}-activated $Sr_5(PO_4)_2(SiO_4)$ for green-emitting phosphor, Mater. Lett. 63 (2009) 2160–2162.

[42] N. Kaltsoyannis, Recent developments in computational actinide chemistry, Chem. Soc. Rev. 32 (2003) 9–16.

[43] S.K. Gupta, N. Pathak, P. Ghosh, R. Kadam, On the photophysics and speciation of actinide ion in $MgAl_2O_4$ spinel using photoluminescence spectroscopy and first principle calculation: A case study with uranium, J. Alloy. Comp. 695 (2017) 337–343.

[44] S.K. Gupta, A. Yadav, S. Nigam, S. Jha, C. Mazumder, D. Bhattacharya, S. Thulasidas, Speciation and site occupancy of uranium in strontium orthosilicate

by photoluminescence and X-ray absorption spectroscopy: A combined experimental and theoretical approach, Spectrochim. Acta Mol. Biomol. Spectrosc. 151 (2015) 453–458.

[45] G. Liu, N.P. Deifel, C.L. Cahill, V.V. Zhurov, A.A. Pinkerton, Charge transfer vibronic transitions in uranyl tetrachloride compounds, J. Phys. Chem. 116 (2012) 855–864.

[46] G. Liu, M. Jensen, Theoretical analysis of optical spectra of uranyl in complexes, Chem. Phys. Lett. 499 (2010) 178–181.

[47] E. van Besien, K. Pierloot, C. Görller-Walrand, Electronic spectra of uranyl chloride complexes in acetone: a CASSCF/CASPT2 investigation, Phys. Chem. Chem. Phys. 8 (37) (2006) 4311–4319.